Pulse Shape Discrimination Algorithms, Figures of Merit, and Gamma-Rejection for Liquid and Solid Scintillators

Willem G. J. Langeveld, Michael J. King, John Kwong, and Daniel T. Wakeford

***Abstract*— Pulse shape discrimination (PSD) in scintillators is useful to distinguish between signals from neutrons and gamma rays. A standard algorithm is to divide the integral of the tail end of the pulse by the total pulse integral, which itself yields the deposited energy. When the PSD ratio is plotted against the energy, two bands emerge for scintillators that respond differently to neutrons and gammas. Often, a figure of merit (FOM) is defined as the distance between the two bands in a particular energy range, divided by the sum of the full-widths at half-maximum of the PSD ratio bands. A high FOM is usually interpreted as a good indicator of how well a certain scintillator device can distinguish between neutrons and gammas. This, however, ignores the actual shape of the two bands, which may not have a Gaussian shape in the direction of the PSD ratio axis, especially in the presence of pulse pileup. Thus, the FOM may not say much about the gamma rejection capability of the detector, and can therefore be a little misleading. Here, we describe the results of research and development performed on a stilbene detector borrowed from the Lawrence Livermore National Laboratory, but the algorithms described were also successfully used on a number of plastic and liquid scintillation detectors. The standard algorithm described above was compared with a newly developed wavelet-based algorithm that is also used to reject pileup, as well as a pulse shape fitting approach which is shown to be capable of significantly improving the gamma-rejection ratio.**

***Index Terms*— Figure of merit (FOM), gamma-rejection, gamma-rejection ratio, pileup-rejection, pulse pileup, pulse shape discrimination (PSD), scintillators.**

I. Introduction

PULSE shape discrimination (PSD) in scintillators is useful to distinguish between signals from neutrons and gamma rays. It is well known that neutrons and gammas tend to produce slightly different signal pulses in certain scintillation materials [1]–[3]. In particular, pulses due to neutrons tend to have a slightly longer tail than those due to gamma rays (see Fig. 1). One standard algorithm for the PSD value is to divide the integral of the tail end of the pulse by the total pulse integral, I_0. Unless mentioned specifically, we assume the pulses to be baseline-subtracted and, if necessary, flipped to produce positive pulses. Here, I_0 is approximately proportional to the deposited energy, and thus, the energy can be obtained from I_0 by calibration. Plotting this PSD value versus energy, two bands emerge for such scintillators. Typically, a figure of merit (FOM) is defined as the distance between the two bands in a particular energy range, divided by the sum of the full-widths at half-maximum (FWHM) of the PSD bands. A high FOM is then interpreted as a good indicator of how well a certain scintillator distinguishes between neutrons and gammas. This, however, ignores the fact that one or both of the two bands may not have a Gaussian shape in the direction of the PSD axis. This is especially true in the presence of pulse pileup, where two pulses arrive at almost the same time, throwing off the simple PSD calculation. Thus, the FOM value may be misleading in regards to the gamma-rejection ratio of the detector, which is defined as the fraction of gammas mistaken for neutrons when only gammas are present.

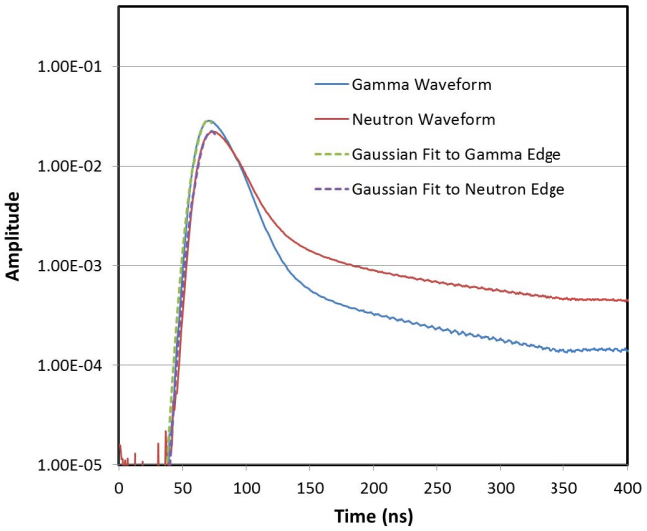

Fig. 1. Averaged waveforms due to gamma rays and neutrons for a stilbene detector. Also shown are Gaussian fits to the leading edges. For this detector, the rise time is approximately 14 ns, dominated by the PMT response and read-out electronics.

Here, we describe a wavelet-based algorithm that is used to calculate a PSD value and to reject pileup at the same

Manuscript received July 1, 2016; revised January 16, 2017; accepted March 7, 2017. Date of publication March 13, 2017; date of current version July 14, 2017. This work was supported by the U.S. Department of Homeland Security, Domestic Nuclear Detection Office under competitively awarded Contract/IAA HSHQDC-10-C-00048 and Contract/IAA HSHQDC-11-C-00092.

W. G. J. Langeveld is with Rapiscan Laboratories, Inc., Sunnyvale, CA 94085 USA (e-mail: wlangeveld@rapiscansystems.com).

M. J. King and J. Kwong were with Rapiscan Laboratories, Inc., Sunnyvale, CA 94085 USA. They are now with Berkeley Applied Analytics, Inc., Berkeley, CA 94704 USA (e-mail: michael.king@berkeleyappliedanalytics.com; john.kwong@berkeleyappliedanalytics.com).

D. T. Wakeford was with Rapiscan Laboratories, Inc., Sunnyvale, CA 94085 USA. He is now with the Los Alamos National Laboratory, Los Alamos, NM 87545 USA (e-mail: wakeford@lanl.gov).

Color versions of one or more of the figures in this paper are available online at http://ieeexplore.ieee.org.

Digital Object Identifier 10.1109/TNS.2017.2681654

time, thereby improving the gamma-rejection ratio. Wavelet methods have been used in the past [4]–[6], where a Haar wavelet is used and the discrimination is in the frequency domain. The method presented here uses a Marr wavelet applied in the time domain, and is less sensitive to mistakes in baseline subtraction. We also describe a pulse shape-fitting approach, similar to the correlation method in [7], capable of significantly improving the gamma-rejection ratio. This approach automatically rejects pileup. We compare the results with a derivative-based approach to pileup-rejection.

Commonly available fast digitizers have a relatively low dynamic range, making accurate measurement of the low-amplitude tail of a pulse difficult while keeping the pulse peak within the range of the digitizer. In Appendix B, we describe a method for approximate recovery of the missing part of a clipped pulse peak, allowing one to exceed the dynamic range on purpose in order to improve the accuracy of measuring the tail of the pulse.

II. Threshold-Based Pileup-Rejection Algorithm

Pileup is the presence, due to high count rates, of more than one gamma or neutron pulse in the part of the waveform used for the PSD measurement.

One possible pileup-rejection algorithm works as follows. Given a sampled (positive) waveform [Fig. 2 (top)], the discrete derivative [Fig. 2 (bottom)] is computed using the differences of two samples that are one or more samples apart along the time axis. From Fig. 2 (bottom), it is clear that the derivative first rises to a high value, and then falls to a low value, crossing zero in between. A threshold value is determined empirically from the noise present in the system and the rise time of the signal (faster detectors have larger values of the derivative). In Fig. 2 (bottom), positive and negative such thresholds are shown by red horizontal lines. Note that use of the derivative eliminates any flat offsets that may be present in the waveform, so the waveform need not be baseline-subtracted.

This pileup-rejection algorithm then counts the number of "flips" present in the derivative, as defined by the number of times the derivative crosses from above the positive threshold to below the negative threshold. If that number is 1 across the entire ("long-gate") time period, there is presumably only one gamma or neutron pulse. If there is more than one such crossing, the waveform may suffer from pileup.

RF or other noise can sometimes trigger the data acquisition system. Such noise signals are typically faster than true detector signals, and thus have larger derivatives and often exhibit significant ringing, leading to a large number of flips. Because of this, typically signals with more than ∼10 crossings can be considered noise signals rather than piled-up signals; piled-up signals usually have less than ∼5 crossings.

III. Wavelet PSD and Pileup-Rejection Algorithm

The continuous wavelet transform (CWT) of a function is a matrix of coefficients, ϕ_{ab}, given by the convolution integral

$$\varphi_{a,b} = \int_{-\infty}^{\infty} f(t)\psi_{a,b}(t)dt \tag{1}$$

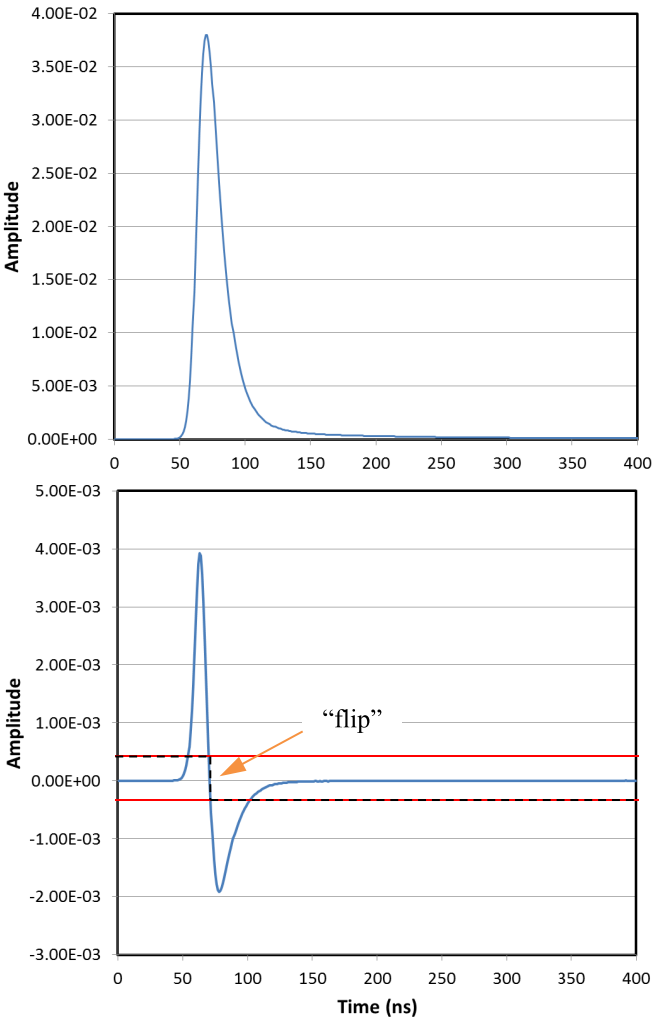

Fig. 2. Top: baseline-subtracted waveform. Bottom: derivative of background-subtracted waveform, Threshold curves (red) define the range the signal must fall through to trigger a "flip."

where

$$\psi_{a,b}(t) = \frac{1}{\sqrt{a}}\psi\left(\frac{t-b}{a}\right). \tag{2}$$

Here, $\psi(t)$ is called the mother wavelet and $\psi_{a,b}(t)$ is the wavelet at scale a and translate b; further $f(t)$ is the function we are studying (here, the waveform, e.g., Fig. 1).

In principle, the scale a and translate b can take any value, which is why this is called the CWT. Since the signal (see Fig. 2) looks much like a Gaussian with a long tail on one side, an appropriate choice for the wavelet function is the Marr (or Mexican-hat) wavelet (Fig. 3), which is the second derivative of a standard Gaussian function

$$\psi(t) = \frac{2}{\sqrt{3\sigma}\,\pi^{\frac{1}{4}}}\left(1-\frac{t^2}{\sigma^2}\right)e^{-\frac{t^2}{2\sigma^2}}. \tag{3}$$

It has the property

$$\int_{-\infty}^{\infty}\psi(t)dt = 0 \tag{4}$$

and $\psi(t)$ is also symmetric. These two properties ensure that the convolution integral yields zero for parts of the waveform

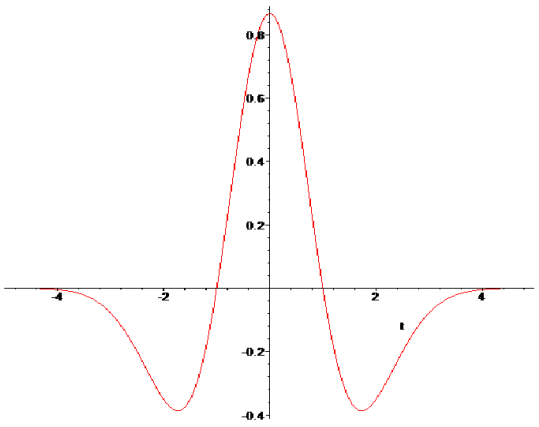

Fig. 3. Marr wavelet.

that are odd functions with respect to the center of the wavelet peak, such as constant or linearly falling or rising components. If the width of the wavelet is chosen to be comparable to the width of the peak of the pulse, the CWT of the waveform will ignore, to a large extent, the long tail. Therefore, a comparison of the CWT, integrated over time and ignoring values less than zero, with the integral of the signal is a pulse shape discriminator in its own right. Defining the wavelet PSD as

$$\mathrm{PSD}_w = \frac{2I_0}{I_0 + I_w} \tag{5}$$

results in PSD plots that are similar to ones obtained using the standard method. Here, I_0 is the integral of the signal, and

$$I_w = \int \max\left(0, \int f(t')\psi_{\sigma,t}(t')dt'\right)dt \tag{6}$$

where $f(t')$ is the waveform and $\psi_{\sigma,t}(t')$ is the wavelet at chosen width (standard deviation) σ and time t. The mother wavelet we use is the Marr wavelet from (3) but with a slightly different normalization and with (its) σ set to $\sqrt{5}$

$$\psi(t) = \frac{18}{5\sqrt{15\pi}}\left(1-\frac{t^2}{5}\right)e^{-\frac{t^2}{10}}. \tag{7}$$

This way, the integral of the CWT of a Gaussian waveform with amplitude A and standard deviation σ, centered at time t_0, reaches a maximum value of $A\sqrt{\sigma}$ for $a = \sigma$ and $b = t_0$, where t_0 is the peak location. For the scale a, we used here the average signal FWHM divided by 2.35.

The CWT can be easily implemented using, e.g., the fast Fourier transform (FFT). After applying the FFT to both the wavelet $\psi(t)$ and to the pulse shape, the convolution is simply the inverse FFT of the product of the two FFTs. The FFT $\tilde{\psi}(\omega)$ of $\psi(t)$ can be precomputed, or computed analytically

$$\begin{aligned}\tilde{\psi}(\omega) &= \mathcal{F}(\psi(t)) = \mathcal{F}\left(\frac{18}{5\sqrt{15\pi}}\left(1-\frac{t^2}{5}\right)e^{-\frac{t^2}{10}}\right)\\ &= 6\sqrt{6}\omega^2 e^{-\omega^2}.\end{aligned} \tag{8}$$

For a note on the use of Marr wavelets see Appendix A. In the data presented in this paper, some of the pulses of high-energy events have been allowed to exceed the ADC dynamic range in order to improve the measurement of the tail. For a derivation of a correction factor for such "clipped" pulses see Appendix B.

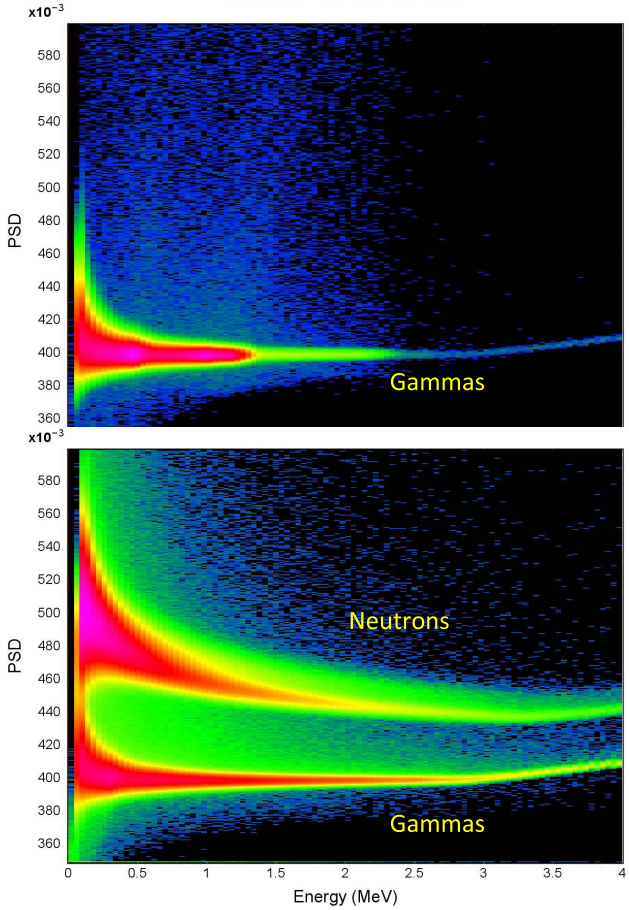

Fig. 4. PSD_w versus energy before cuts. Top: ^{137}Cs and ^{60}Co sources. Bottom: ^{252}Cf source. The intensity scale is heavily compressed.

A. Wavelet-Based PSD

We now plot PSD_w as a function of energy for two data sets taken with a stilbene detector borrowed from the Lawrence Livermore National Laboratory, one set obtained with ^{137}Cs and ^{60}Co gamma ray sources and the other with a ^{252}Cf mixed gamma/neutron source [see Fig. 4 (top and bottom)]. The intensity scale of Fig. 4 is heavily compressed to show background pulses. The blue background at high PSD value is largely due to pileup. Note that the energy scale uses the correction for clipped pulses discussed in Appendix B, but the PSD_w calculation uses the uncorrected pulse integral I_0.

B. Wavelet-Based Pileup-Rejection

Fig. 5 shows a 2-D cumulative plot of the wavelet transform of the waveforms used in Fig. 4 (bottom), each of which was normalized to the total integral I_w. The vertical scale thus represents the contribution of the wavelet-transformed waveform to I_w, as a function of translated time. Clearly, I_w gets most of its (positive) contributions from channels ~50 to ~110 and would have smaller but negative contributions in the tail, but we reject those contributions in (6).

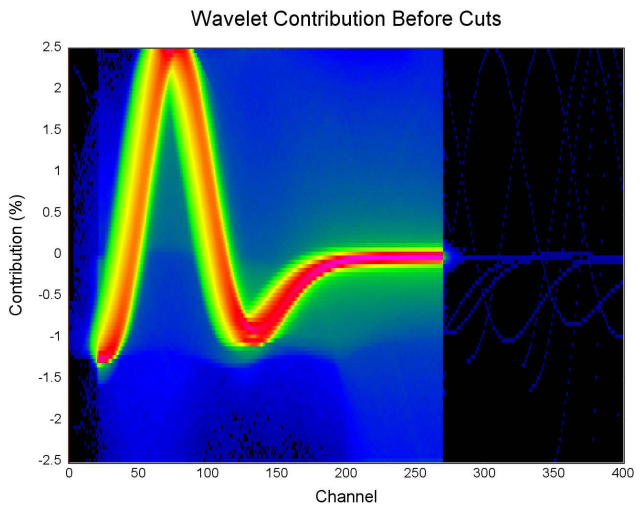

Fig. 5. Normalized wavelet transform of signals before cuts.

The blue haze in the plot is caused by pileup. It is, therefore, possible to reject this pileup by removing all events whose CWTs have positive or negative contributions above some channel number. In the example presented here, we reject events with contributions less than -0.5 above channel 175 and those with contributions greater than 0.1 above channel 120. The PSD and contribution plots with that cut (and a few other cuts that are of no consequence for this discussion) are shown in Figs. 6 and 7, respectively. We can see that the cleanup of Fig. 7 as compared with Fig. 5 is substantial, and this results in the removal of a lot of blue scatter in Fig. 6 as compared with Fig. 4.

We can compare the effectiveness of the wavelet-based pileup cut with that of the simple algorithm discussed earlier: For Fig. 4 (bottom) the simple algorithm removes about 81 000 events out of about 35 million, whereas the wavelet algorithm removes ∼163 000, more than twice as many. This may be because it is easier to decide on cuts in the wavelet algorithm.

C. Figure of Merit

A standard algorithm for the FOM of gamma-neutron separation is given as

$$\mathrm{FOM} = \frac{\mathrm{PSD(Neutron)} - \mathrm{PSD(Gamma)}}{\mathrm{FWHM(Neutron)} + \mathrm{FWHM(Gamma)}}. \quad (9)$$

One starts by projecting a certain energy region of a PSD plot (e.g., Fig. 6) onto the vertical (PSD) axis, resulting in two peaks. In (9), PSD(…) then stands for the PSD value of the corresponding peak location, and FWHM(…) for the full-width at half-maximum of that peak. Such a projection is depicted in Fig. 8. The blue solid line in Fig. 8 is a projection of the energy range 0.5–4.0 MeV onto the PSD axis for Fig. 4 (top), i.e., for gamma rays without the pileup-rejection cut, and the red solid line is the same for Fig. 6 (top), i.e., after applying the cut. Similarly, the green and purple dotted lines are for a mixture of gamma and neutron signals from Fig. 4 (bottom) and Fig. 6 (bottom). Note the logarithmic vertical scale.

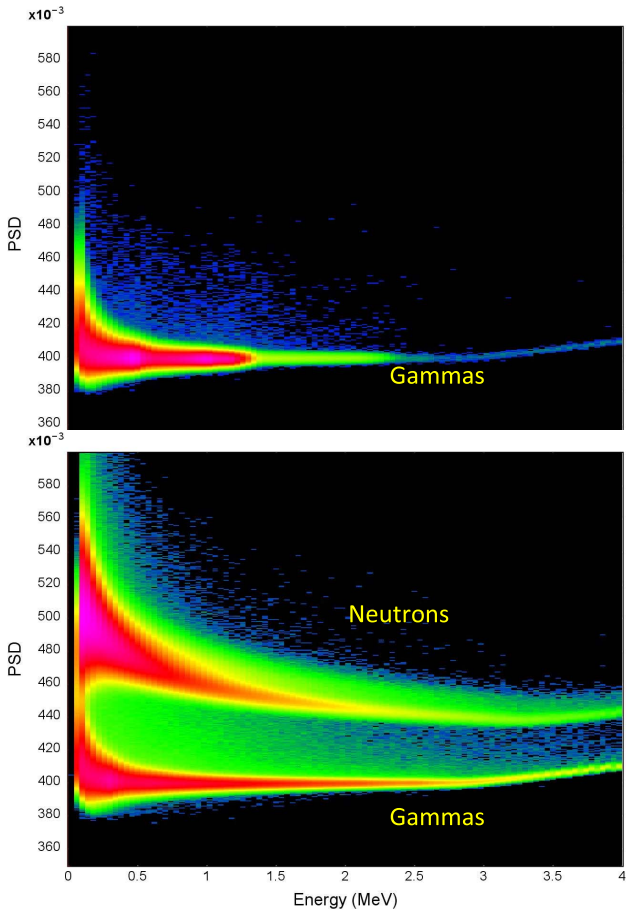

Fig. 6. PSD_w versus energy after cuts. Top: ^{60}Co source. Bottom: ^{252}Cf source.

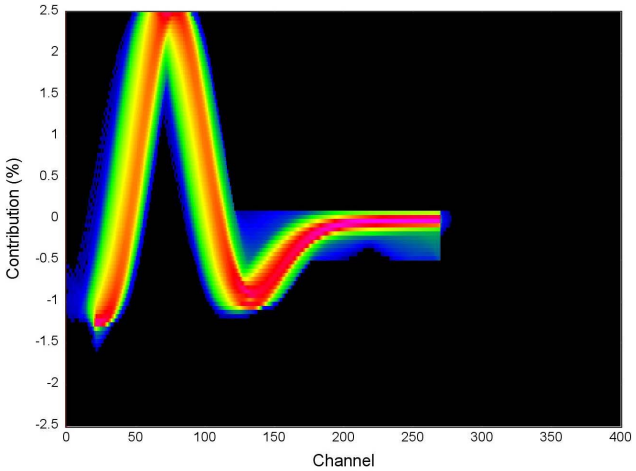

Fig. 7. Normalized wavelet transform of signals after cuts.

Fig. 9 shows the FOM as a function of energy for the stilbene detector. The standard pileup-rejection algorithm (red line) corrects for the missing energy due to clipped pulses, and thus assigns energies above ∼2 MeV more-or-less correctly and produces good FOMs above 3.5 MeV, a region that would not be accessible without clipped-pulse correction. The energy correction, however, introduces an additional uncertainty which broadens the PSD distributions

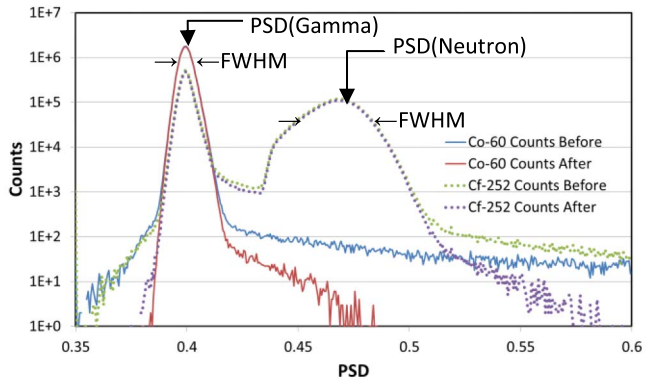

Fig. 8. PSD projection of the energy region 0.5–4 MeV for gamma events (solid lines) and for mixed gamma and neutron events (dotted lines), with and without cuts.

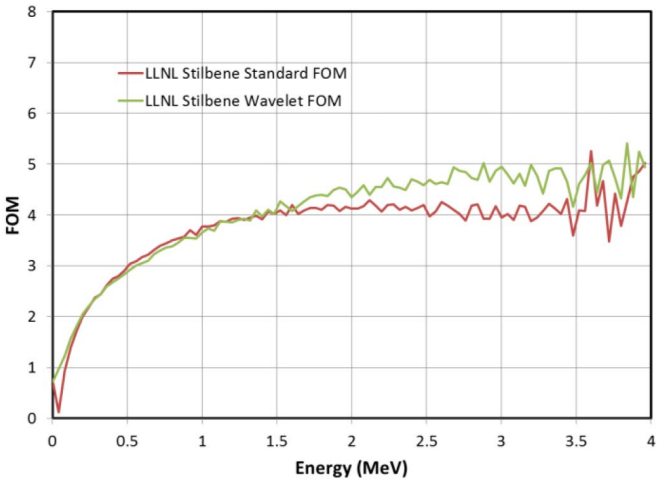

Fig. 9. Comparison of PSD methods for stilbene detector.

slightly at energies where the signals are clipped, resulting in FOMs that are somewhat lower than the rising trend one might expect. The wavelet algorithm (green line) does not correct for missing energy in the PSD calculation but does use the corrected overall energy determination. As can be seen from the graph, it produces roughly the same FOM as the standard algorithm below ∼1.5 MeV, and a better FOM above 1.5 MeV. The FOMs displayed in Fig. 9 are calculated from PSD plots made after various cuts, including the pileup cut. The difference between the FOMs before and after pileup cuts is, however, insignificant, since the FWHM is measured well above the pileup tails, as approximately indicated in Fig. 8. Table I lists the FOMs at a number of different energies for the two methods.

D. Gamma-Rejection Ratio

We next study the effect of pileup-rejection on the gamma-rejection ratio. As noted earlier, definition (9) of the FOM is insensitive to tails in the distribution, and a good FOM does not imply good gamma-rejection. For example, purely Gaussian PSD distributions with no tails result in high-gamma-rejection when looking for neutrons, whereas non-Gaussian shapes with large tails would result in poor gamma-rejection.

TABLE I
STILBENE FOMS AT VARIOUS ENERGIES FOR THE TWO PSD METHODS

Energy (MeV)	FOM (Standard)	FOM (Wavelet)
0.1 (0.08 - 0.12)	1.16	1.40
0.5 (0.48 - 0.52)	2.97	2.88
1.0 (0.98 - 1.02)	3.72	3.64
2.0 (1.96 - 2.04)	4.14	4.44
3.0 (2.96 - 3.04)	4.05	4.87

The difference between the gamma-ray data in Fig. 4 (top) and Fig. 6 (top) is largely due to the pileup cut. Here, the wavelet-based pileup cut removes ∼53 000 out of ∼37 million events, whereas the simple pileup cut would only have removed ∼40 000.

This is reflected in Fig. 8. For the gamma-source run (solid curves), a significant number of events are removed above about a PSD value of 0.42, and in particular in the region between PSD values of 0.44 and 0.5 where any neutrons would be expected (as shown by the dotted curves). For this case, we calculate a gamma-rejection ratio of 1 in ∼3000 without any cuts, and 1 in ∼32 000 with the wavelet-based pileup cut, i.e., more than a factor of 10 better. The gamma-rejection ratios are slightly better in some energy ranges than in others, since tighter neutron regions can be used. For example, in the energy range 0.5–1.0 MeV, one can restrict the neutron PSD to the range 0.45–0.5, and the gamma-rejection ratio then is 1 in ∼70 000 after the cut. On the other hand, between 1 and 2 MeV, the gamma-rejection ratio is 1 in ∼27 000 for neutron PSDs between 0.44 and 0.5.

It is further clear that one can improve the gamma-rejection ratio by reducing neutron detection efficiency. Using the energy range 0.5–1.0 MeV as an example, if one chooses to only look for neutrons with a PSD above 0.47 (rather than 0.45), the gamma-rejection ratio improves another factor of 5, to 1 in ∼365 000, at the cost of rejecting about 44% of the neutrons.

The fact that pileup-rejection leads to significantly better gamma-rejection ratios is clearly demonstrated. Note that pileup does not have to be very frequent to constitute a significant problem; here the ∼53 000 pileups out of ∼37 000 000 events constitute only 0.14% of events, yet rejection of the piled-up events can improve the gamma-rejection ratio by more than an order of magnitude.

IV. PULSE SHAPE FITTING

Somewhat similar to the correlation method from [7], the idea behind pulse shape fitting is to find reference pulse shapes for gamma rays and neutrons by averaging many pulses of known origin, and to compare those known signal shapes to individual signals by using chi-squared fits to both hypotheses. The two chi-squares are likely to be different, and if the chi-squared is significantly lower for one hypothesis than for the other, the pulse is assigned to that category. If both chi-squares are larger than some predetermined value, the pulse is discarded on the grounds that it fits neither hypothesis. That could, for example, be the case if there is pulse pileup, so this method inherently rejects pileup. A possible problem with

this method is that the scintillator decay time can depend on temperature [8]. On the other hand, significant improvement of the gamma-rejection ratio may well require environmental conditioning of the scintillator material in general.

A. Algorithm

In practice, pulse shape fitting is somewhat complicated. The chi-squared of the fit is defined as

$$\chi^2 = \sum_{i=1}^{n} \frac{(y_i - Af(t_i - t_{\text{offset}}))^2}{\delta y_i^2} \tag{10}$$

where y_i are the individual pulse sample values at times t_i, $f(t)$ is the fitting function (here either the reference gamma or neutron pulse shape), A a proportionality factor to be fit, and t_{offset} an offset in the time direction. The δy_i are the uncertainties in the sample values y_i, but since we usually do not know what they are, we will set them to one, meaning that all sample values contribute equally to the chi-squared.

The chi-squared will be at a minimum if A is equal to the pulse amplitude, assuming the reference pulse shapes are normalized to have unit amplitude, and if the time offset correctly matches the pulse and reference pulse peak locations. The peak location is not exactly known, since it tends to shift depending on the pulse amplitude if a fixed trigger level is used, as was the case with the data presented here. The offset could potentially be predetermined if a constant-fraction discriminator was to be used.

For a given offset t_{offset}, the value of A can be determined using the linear-least-squares method, by setting the derivative of χ^2 with respect to A to zero

$$\frac{\partial}{\partial A}\chi^2 = \sum_{i=1}^{n} 2(y_i - Af(t_i - t_{\text{offset}}))f(t_i - t_{\text{offset}}) = 0. \tag{11}$$

This leads to a simple formula for A

$$A = \frac{\sum_{i=1}^{n} y_i f(t_i - t_{\text{offset}})}{\sum_{i=1}^{n} f(t_i - t_{\text{offset}})^2}. \tag{12}$$

The chi-squared per degree of freedom can then be written as

$$\chi^2_{\text{pdf}} = \frac{1}{n-1}\left\{\left(\sum_{i=1}^{n} y_i^2\right) - \frac{\left\{\sum_{i=1}^{n} y_i f(t_i - t_{\text{offset}})\right\}^2}{\sum_{i=1}^{n} f(t_i - t_{\text{offset}})^2}\right\}. \tag{13}$$

If the offset t_{offset} is not given, there is a problem. Setting the derivative of χ^2 with respect to t_{offset} to zero yields

$$\sum_{i=1}^{n} y_i f'(t_i - t_{\text{offset}}) = \sum_{i=1}^{n} Af(t_i - t_{\text{offset}})f'(t_i - t_{\text{offset}}). \tag{14}$$

While we can substitute (12) into this to arrive at an equation for t_{offset} only, (14) depends nonlinearly on t_{offset}, and also on the derivative of $f(t)$, denoted by $f'(t)$. Generally, both A and t_{offset} can be determined simultaneously using more complicated fitting algorithms, such as steepest gradient searches and simplex methods, but these do not easily lend themselves for a fast implementation.

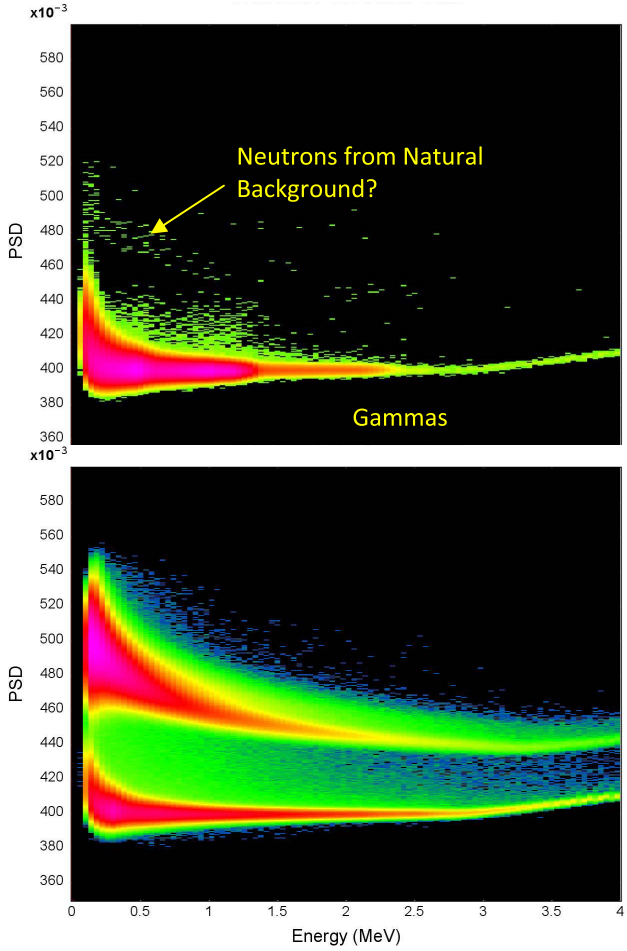

Fig. 10. PSD_w for gamma-source data (top) and neutron source data (bottom) with pulse shape fitting cut.

We can use an approximation for t_{offset} by first assuming $t_{\text{offset}} = 0$, and then varying it by a few time bins in both directions to determine which choice of t_{offset} yields the lowest χ^2_{pdf}. The corresponding value of A then yields the amplitude.

B. Pulse Shape-Fitting Cut

We apply the entire procedure for each reference pulse shape, and obtain two chi-squared values, one for the gamma fit and one for the neutron fit. If both chi-squared values are greater than some maximum allowable value (determined empirically), the pulse is rejected. We find that a constant multiplied by the square of the energy (as determined from the pulse integral) yields a maximum allowable value that works well for the entire energy range. This is due to the fact that the chi-squared is quadratic in the pulse height (and therefore in the energy), since the uncertainties δy_i^2 in the chi-squared definition were set to unity.

It is now possible to define a PSD value using the two chi-squared values. One could then plot this, find two lobes, one for neutrons, and one for gammas, and define an FOM, analogously to previous methods.

On the other hand, one can also use the requirement that at least one of the chi-squared values is below the maximum

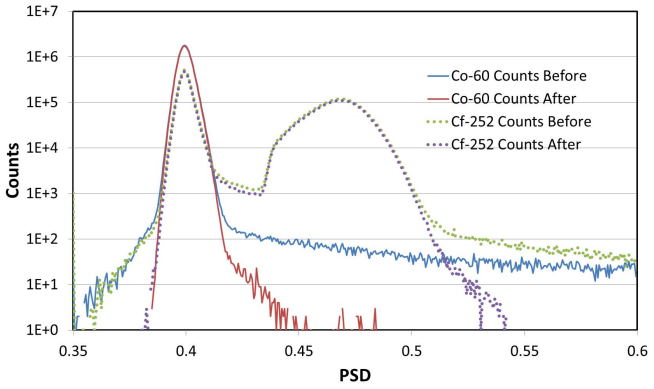

Fig. 11. PSD projections for energies between 0.5 and 4 MeV for gamma events (solid lines) and for mixed gamma and neutron events (dotted lines), with and without the pulse shape fitting cut.

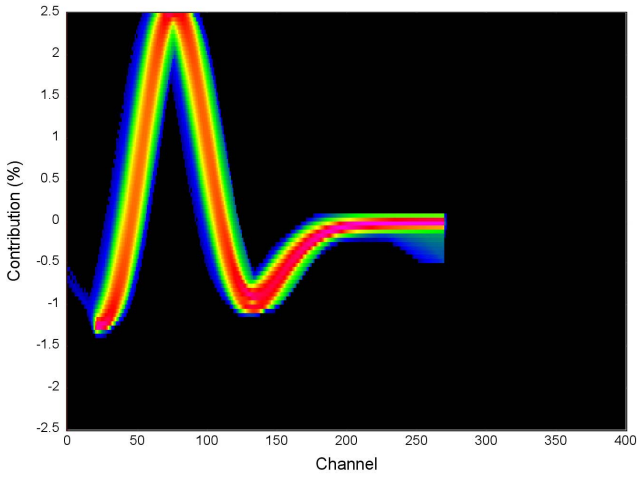

Fig. 12. Normalized wavelet transforms for pulses after the pulse shape-fitting cut.

allowable value and use this simply as a cut. We can then plot the wavelet PSD as defined before versus the energy with this cut [see Fig. 10 (top)]. The scattered entries have been reduced compared with Fig. 6 (top). In fact, the remaining data points in the band near a PSD value of 480 may be due to neutrons from natural background.

Fig. 10 (bottom) shows the same for the ^{252}Cf data. Although scattered entries above and below the two bands have been reduced compared with Fig. 6 (bottom), there are still a significant number of entries between the two bands. These must, therefore, be due to neutrons, but we do not have a full explanation for these events. One suggested possibility [9] is that these events are due to neutrons with incomplete deposition of proton recoil energy, which might occur near the edges of the detector.

Fig. 11 shows the PSD projections in the energy range 0.5–4 MeV. The gamma-rejection ratio with cuts is 1 in ~210 000 for neutron PSDs between 0.44 and 0.5, and about 4% of events are rejected. Again, this can be improved by using smaller energy ranges.

For example, in the energy range 0.5–1 MeV, the gamma-rejection ratio is 1 in ~420 000 for neutron PSDs

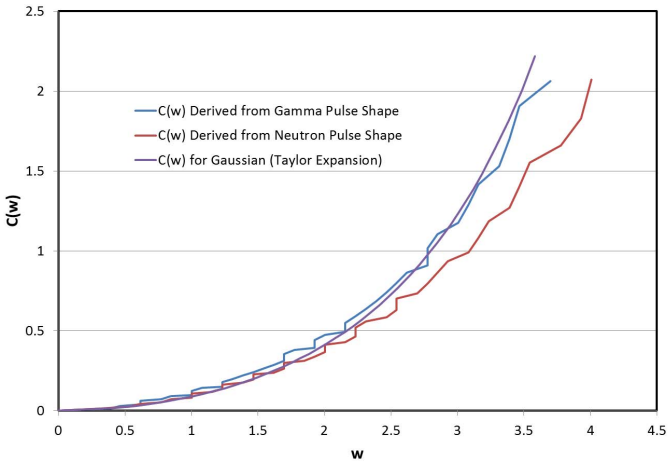

Fig. 13. Correction factor $C(w)$ as a function of w, as computed from known stilbene gamma and neutron pulse shapes, and from the Gaussian approximation.

between 0.45 and 0.5. The actual gamma-rejection ratios may be better, because, as mentioned, the numbers presented here may include some real neutrons from backgrounds.

In sum, the pulse shape fitting algorithm is effective in improving the gamma-rejection ratio, with relatively few rejected events. Because of the nature of the method, pileup-rejection is implicit, as can be seen from a comparison of the normalized wavelet transform contribution plot in Fig. 12 to the one without cuts, Fig. 5. In this analysis, no other pileup-rejection cuts were applied.

C. Pulse Shape Fitting With Clipped Pulses

The above outlined algorithm works with full pulse shapes, i.e., pulses that fit within the range of the digitizer. It also works with clipped pulse shapes, as long as the clipped region is not used in the determination of the chi-squared. Estimation of the peak offset t_{offset} is a little more cumbersome. We start by defining a trial offset $t_{\text{trial-offset}}$ as the center of the clipped region, and then continue, as before, by varying $t_{\text{trial-offset}}$ by a few time bins in both directions to determine which choice of $t_{\text{trial-offset}}$ yields the lowest χ^2_{pdf}. The rest proceeds as before, except that we use the clipped-pulse correction from Appendix B for determining the energy.

V. Conclusion

We have described a wavelet-based method for PSD and pileup-rejection. We show that this improves the FOM at high energies but arguably only marginally, compared with standard methods. But, as we have pointed out, the FOM is not a good measure of gamma-rejection, especially if the PSD projections are non-Gaussian. The gamma-rejection ratio is, however, improved considerably compared with that obtained using previous methods.

The main advantages of the wavelet approach are that pileups are identified very easily, and in the same procedure which also provides a superior PSD calculation. On the other hand, in the simple PSD method, the PSD is calculated using a somewhat arbitrary tail definition and the pileup-rejection method is entirely separate with its own set of

adjustable parameters. Furthermore, the simple PSD method is sensitive to baseline shifts, whereas the (Marr) wavelet method is not.

We have also demonstrated a pulse shape fitting approach capable of further improving the gamma-rejection ratio. In addition, we have provided a correction procedure for clipped pulses which can be used to improve measurement of the tail.

Appendix A
Note on Marr Wavelets

The Marr wavelet is proportional to the second derivative of a Gaussian

$$\psi(t) \propto \frac{\partial^2}{\partial t^2} g(t) \tag{15}$$

where we set $t_0 = 0$. Thus, the convolution from (1)

$$\varphi_{a,b} = \int_{-\infty}^{\infty} f(t)\psi_{a,b}(t)dt \tag{16}$$

can also be written as

$$\varphi_{a,b} \propto \int_{-\infty}^{\infty} f(t) \left\{ \frac{\partial^2}{\partial t^2} g_{a,b}(t) \right\} dt \tag{17}$$

with $g_{a,b}(t)$ defined in analogy to $\psi_{a,b}(t)$

$$g_{a,b}(t) = \frac{1}{\sqrt{a}} g\left(\frac{t-b}{a}\right). \tag{18}$$

Integrating (17) by parts we get

$$\begin{aligned} \varphi_{a,b} &\propto \int_{-\infty}^{\infty} f(t) d\left\{ \frac{\partial}{\partial t} g_{a,b}(t) \right\} \\ &= f(t) \frac{\partial}{\partial t} g_{a,b}(t) \Big|_{-\infty}^{\infty} - \int_{-\infty}^{\infty} \frac{\partial}{\partial t} f(t) \frac{\partial}{\partial t} g_{a,b}(t) dt. \end{aligned} \tag{19}$$

The first term vanishes since $g_{a,b}(t)$ and its derivatives vanish at infinity. We can repeat the procedure to obtain

$$\varphi_{a,b} \propto \int_{-\infty}^{\infty} \left\{ \frac{\partial^2}{\partial t^2} f(t) \right\} g_{a,b}(t) dt. \tag{20}$$

This shows that, in essence, the CWT with a Marr wavelet is equivalent to convolution of the second derivative of the function $f(t)$ with a Gaussian, i.e., the Marr wavelet convolution simply results in the blurred second derivative of $f(t)$. The second derivative of $f(t)$ on the other hand, by definition, removes any constant offset to the function, as well as any linear contributions, yielding another explanation of why the CWT of the waveform using a Marr wavelet emphasizes the peak of the pulse and largely ignores the tail.

Appendix B
Clipped-Pulse Correction

Typical neutron and gamma pulse shapes, as shown in Fig. 1, are only obtained if their amplitude is small enough to fit inside the range of the digitizer used. Thus, often the gain of the preamplifier (if used) in the system has to be reduced in order to accommodate the largest (i.e., highest energy) gamma and/or neutron pulses. Given a certain limited number of bits available in the ADC, gain reduction then leads to lower accuracy in digitizing the tail of the pulse. This, combined with the overall electronics noise level seen by the digitizer, can then lead to lower accuracy in the PSD determination.

Gain reduction is, however, not absolutely necessary: one can obtain acceptable results even from "clipped" pulses, i.e., those that exceed the dynamic range of the ADC.

We define the width w of the clipped section in terms of the FWHM of the pulse as

$$w \equiv \frac{2.35\ N}{\text{FWHM}} \tag{21}$$

where N is the number of sample channels where the pulse is clipped, and the FWHM is also measured in number of channels. With this definition, one can obtain the full integral I_{full} of the pulse, given the integral I_0 as defined earlier and the integral of the clipped region only, $I_{\text{clipped-region}}$, as follows:

$$I_{\text{full}} = I_0 + C(w) I_{\text{clipped-region}}. \tag{22}$$

The correction factor $C(w)$ can be calculated exactly for an ideal Gaussian-shaped pulse. We start from the formula for a Gaussian, normalized such that the peak value is 1

$$g(t) = e^{-\frac{t^2}{2\sigma^2}}. \tag{23}$$

Solving the equation $g(t) = A$ for t yields

$$\pm t_c = \pm\sigma\sqrt{-2\ln A} \tag{24}$$

which, obviously, only has real solutions for $A < 1$. Thus, the width of the clipped region is

$$2t_c = 2\sigma\sqrt{-2\ln A} \equiv w\sigma \tag{25}$$

where we define w as the width measured in units of σ. The measured integral of the clipped region is simply

$$I_{\text{measured}} = 2A\sigma\sqrt{-2\ln A}. \tag{26}$$

The integral of the Gaussian shape in that region is, however

$$I_{\text{clipped-region}} = \int_{-\sigma\sqrt{-2\ln A}}^{+\sigma\sqrt{-2\ln A}} e^{-\frac{t^2}{2\sigma^2}} dt = \sigma\sqrt{2\pi}\,\text{erf}(\sqrt{-\ln A}). \tag{27}$$

The correction factor for the clipped region-only is then

$$F = \frac{I_{\text{clipped-region}}}{I_{\text{measured}}} = \frac{\sqrt{2\pi}\,\text{erf}(\sqrt{-\ln A})}{2A\sqrt{-\ln A}}. \tag{28}$$

We can write this alternatively using (23) and the definition of w in (25)

$$A = e^{-\frac{t_c^2}{2\sigma^2}} = e^{-\frac{w^2}{8}} \tag{29}$$

leading to

$$F = \frac{\sqrt{2\pi}}{w}\text{erf}\left(\frac{\sqrt{2}}{4}w\right)\exp\left(\frac{w^2}{8}\right). \tag{30}$$

Since the full integral I_0 already includes the integral of the clipped region once, the correction factor for just the clipped-region integral is

$$C(w) = F - 1 = \frac{\sqrt{2\pi}}{w}\text{erf}\left(\frac{\sqrt{2}}{4}w\right)\exp\left(\frac{w^2}{8}\right) - 1. \tag{31}$$

The desired full integral is then given by (22). The Taylor expansion of the expression on the right in (31) is

$$C(w) = \frac{1}{12}w^2 + \frac{1}{240}w^4 + \frac{1}{6,720}w^6 + \frac{1}{241,920}w^8 + \frac{1}{10,644,480}w^{10} + \dots \quad (32)$$

which can be rewritten as

$$C(w) = \frac{w^2}{12}\left(1 + \frac{w^2}{20}\left(1 + \frac{w^2}{28}\left(1 + \frac{w^2}{36}\left(1 + \frac{w^2}{44}(1 + \dots)\right)\right)\right)\right). \quad (33)$$

The Taylor expansion can reasonably be cut off after the terms shown.

Equation (33) was derived for a Gaussian pulse shape, and we, therefore, need to justify applying it to pulse shapes such as those shown in Fig. 1. We first note that the leading edge itself is well-described by a Gaussian, as can be seen from the Gaussian fit to the leading edges, shown in Fig. 1 as dashed lines. We state without proof that the trailing edge (not including the long tail) is also approximately Gaussian, in particular near the top where clipping would first occur. The standard deviation of the trailing edge is, however, usually larger than that of the leading edge. These considerations lead us to the following approximate procedure. First, we determine the FWHM of the gamma and neutron pulse shapes seen by the detector for those pulses that are not clipped. We then simply apply (21)–(33), as if the pulse shape were Gaussian. Using known unclipped pulse shapes for gammas and neutrons, we then simulate what would happen if they were clipped, and check that the approximation is adequate.

The correction factor $C(w)$ is plotted versus w for pulse shapes measured with the stilbene detector in Fig. 13. Good agreement between the Gaussian assumption and results based on the actual gamma pulse shape is seen up to $w \sim 3.5$, and for those based on the actual neutron pulse shape up to about $w \sim 2.5$. For comparison, $w = 2.5$ corresponds to pulse clipping at $\sim$45% of the peak value, and $w = 3.5$ to clipping at $\sim$20% of the peak value. Thus, allowing pulses to be clipped at, e.g., 25% of their peak value, a factor four (or, equivalently, two bits) of digitizer accuracy is gained.

ACKNOWLEDGMENT

The authors would like to thank the Lawrence Livermore National Laboratory for the use of their stilbene detector. W. Langeveld would like to thank Dr. P. Schuster for his helpful discussions. This support does not constitute an express or implied endorsement on the part of the Government.

REFERENCES

[1] L. Varga, "Pulse shape discrimination," *Nucl. Instrum. Methods*, vol. 14, pp. 24–32, Jan. 1962.
[2] M. L. Roush, M. A. Wilson, and W. F. Hornyak, "Pulse shape discrimination," *Nucl. Inst. Methods*, vol. 31, no. 1, pp. 112–124, Dec. 1964.
[3] P. Chandrikamohan, T. A. DeVol, "Comparison of pulse shape discrimination methods for phoswich and CsI:Tl detectors," *IEEE Trans. Nucl. Sci.*, vol. 54, no. 2, pp. 398–403, Apr. 2007.
[4] S. Yousefi, L. Lucchese, and M. D. Aspinall, "Digital discrimination of neutrons and gamma-rays in liquid scintillators using wavelets," *Nucl. Instrum. Methods Phys. Res. A, Accel. Spectrom. Detect. Assoc. Equip.*, vol. 598, no. 2, pp. 551–555, Jan. 2009.
[5] S. Yousefi and L. Lucchese, "A wavelet-based pulse shape discrimination method for simultaneous beta and gamma spectroscopy," *Nucl. Instrum. Methods Phys. Res. A, Accel. Spectrom. Detect. Assoc. Equip.*, vol. 599, no. 1, pp. 66–73, Feb. 2009.
[6] S. Yousefi, "Digital pulse shape discrimination methods for triple-layer phoswich detectors using wavelets and fuzzy logic," Ph.D. dissertation, Dept. Math., Oregon State Univ., Corvallis, OR, USA, 2008.
[7] T. L. White and W. H. Miller, "A triple-crystal phoswich detector with digital pulse shape discrimination for alpha/beta/gamma spectroscopy," *Nucl. Instrum. Methods Phys. Res. A, Accel. Spectrom. Detect. Assoc. Equip.*, vol. 422, nos. 1–3, pp. 144–147, Feb. 1999.
[8] G. F. Knoll, *Radiation Detection and Measurement*. New York, NY, USA: Wiley, 2000.
[9] P. Schuster, private communication, May 2016.